ARTICLE OPEN

Check for updates

Ab initio molecular dynamics and materials design for embedded phase-change memory

Liang Sun[1,8], Yu-Xing Zhou[2,3,7,8], Xu-Dong Wang[2,3], Yu-Han Chen[2,3], Volker L. Deringer[4], Riccardo Mazzarello[5,6] and Wei Zhang[2,3]✉

The $Ge_2Sb_2Te_5$ alloy has served as the core material in phase-change memories with high switching speed and persistent storage capability at room temperature. However widely used, this composition is not suitable for embedded memories—for example, for automotive applications, which require very high working temperatures above 300 °C. Ge–Sb–Te alloys with higher Ge content, most prominently $Ge_2Sb_1Te_2$ ('212'), have been studied as suitable alternatives, but their atomic structures and structure–property relationships have remained widely unexplored. Here, we report comprehensive first-principles simulations that give insight into those emerging materials, located on the compositional tie-line between $Ge_2Sb_1Te_2$ and elemental Ge, allowing for a direct comparison with the established $Ge_2Sb_2Te_5$ material. Electronic-structure computations and smooth overlap of atomic positions (SOAP) similarity analyses explain the role of excess Ge content in the amorphous phases. Together with energetic analyses, a compositional threshold is identified for the viability of a homogeneous amorphous phase ('zero bit'), which is required for memory applications. Based on the acquired knowledge at the atomic scale, we provide a materials design strategy for high-performance embedded phase-change memories with balanced speed and stability, as well as potentially good cycling capability.

npj Computational Materials (2021)7:29 ; https://doi.org/10.1038/s41524-021-00496-7

INTRODUCTION

With increasing global demand for data storage and processing, massive efforts are underway to develop new electronic devices and platforms, including non-volatile memory and neuro-inspired computing technologies[1–3]. Chalcogenide phase-change materials (PCMs) are leading candidates to implement these functionalities. Phase-change random access memory (PRAM) is programmed to switch between the amorphous and crystalline states of PCMs reversibly and rapidly, and the pronounced contrast in electrical resistance (over three orders of magnitude) or optical reflectance (over 30%) between the two states is used to encode data[1–3]. Competitive storage-class memory products based on PCMs—known as 3D Xpoint—have entered the global memory market recently, largely boosting computing efficiencies by bridging the performance gap between dynamic random access memory (DRAM) and flash-memory-based solid state hard drives (SSD). The core material in use is the $Ge_2Sb_2Te_5$ alloy, located at the midpoint of the GeTe–Sb_2Te_3 pseudo-binary line[4]. As-deposited $Ge_2Sb_2Te_5$ thin films show a crystallization temperature T_x of ~150 °C, and a minimum switching time of ~10 ns in state-of-the-art devices[5,6]. Neuro-inspired computing utilizes the multilevel storage capability of $Ge_2Sb_2Te_5$, making it possible to process data directly within the memory arrays. For a given artificial intelligence (AI) computing task, such as pattern classification, $Ge_2Sb_2Te_5$ based memory arrays were shown to improve the computing, energy, and areal efficiencies by one to two orders of magnitude compared to current computing hardware[7,8].

Moving towards the Sb_2Te_3 end of the compositional pseudo-binary line, the switching speed is further improved, but the amorphous-phase stability is weakened, with a T_x as low as 85 °C[9]. Ab initio materials screening studies have recently shown that alloying with a suitable element, such as Sc[10–15] or Y[16–19], can largely increase the nucleation rate to improve switching speed at elevated temperatures. The recently designed $Sc_{0.2}Sb_2Te_3$ (SST) alloy brings the programming time down to ~0.7 ns, expanding the capability of PRAM for cache-type memory applications[10–15]. The stability of amorphous Sb_2Te_3 thin films can also be improved by alloying with Sc, leading to a T_x of about 150 °C—due to an increase in viscosity, and thus a decrease in growth rate, at low temperatures[10–12]. For high-performance neuro-inspired computing, the spontaneous structural relaxation of amorphous GST is the major obstacle, causing the well-known issue of resistance drift[20]. In ref. [21], it was shown how this issue can be resolved: by the design of a heterostructure that confines amorphous Sb_2Te_3 nanolayers between robust non-PCM $TiTe_2$ crystalline nanolayers, enabling memory operation with nine accurate resistance states. The computing and energy efficiencies of phase-change neuro-inspired computing are expected to be further improved using this new heterostructure alloy[22].

Storage-oriented applications, such as embedded memories, require PCMs with higher amorphous-phase stability at (very) high temperature. This is important, for instance, in the automotive industry, where the ability of the material to endure high operating temperatures outweighs an associated reduction in switching speed[23,24]. Resistance drift is also not an issue for binary storage based embedded memories, as the resistance window widens with time (making the contrast larger and the distinction between 'ones' and 'zeroes' clearer). Two major approaches to create high-temperature stable PCMs include heavy alloying of nitrogen and carbon[25–27], as well as the compositional tuning of Ge–Sb–Te materials (abbreviated as GST in the following) away

[1]Key Laboratory of Materials Processing Engineering, College of Materials Science and Engineering, Xi'an Shiyou University, Xi'an, China. [2]Center for Alloy Innovation and Design (CAID), State Key Laboratory for Mechanical Behavior of Materials, Xi'an Jiaotong University, Xi'an, China. [3]Materials Studio for Neuro-inspired Computing, School of Materials Science and Engineering, Xi'an Jiaotong University, Xi'an, China. [4]Department of Chemistry, Inorganic Chemistry Laboratory, University of Oxford, Oxford, UK. [5]Institute for Theoretical Solid-State Physics, JARA-FIT and JARA-HPC, RWTH Aachen University, Aachen, Germany. [6]Department of Physics, Sapienza University of Rome, Rome, Italy. [7]Present address: Department of Chemistry, University of Oxford, Oxford, UK. [8]These authors contributed equally: Liang Sun, Yu-Xing Zhou. ✉email: wzhang0@mail.xjtu.edu.cn

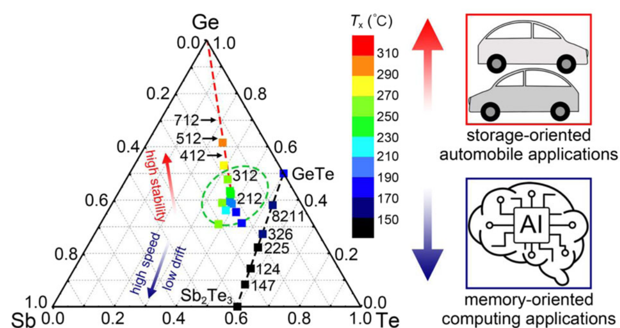

Fig. 1 Ge–Sb–Te ternary diagram. Crystallization temperatures T_x as a function of composition in the Ge–Sb–Te ternary phase diagram. This overview figure is drawn with data from refs [30,34–36], where these values were experimentally determined using as-deposited thin films. Two dashed lines are shown, including the pseudo-binary line (black) between Sb_2Te_3 and GeTe, and the tie-line (red) connecting $Ge_2Sb_1Te_2$ and Ge. GST alloys approaching the Sb_2Te_3 endpoint (blue arrow) are most suitable for memory-oriented applications with high switching speed or for neuro-inspired computing with low resistance drift, while those approaching Ge-rich regions (red arrow) are better suited for storage-oriented applications that primarily require high amorphous-phase stability. Our ab initio simulations indicate an optimal compositional range, as marked by the green dashed line, for high-performance embedded phase-change memories.

from the GeTe–Sb_2Te_3 pseudo-binary line. A so-called 'golden composition'—$Ge_2Sb_1Te_2$—was proposed several years ago, which showed a high $T_x \sim 250$ °C with still quite fast speed ~80 ns[28,29]. Upon further enrichment in Ge content, T_x can reach ~350 °C but with a much slower crystallization speed[28,29]. It was demonstrated that Ge-rich GST alloys function well in integrated memory chips at 190 °C over 10^8 operation cycles[28], making them suitable for automotive micro-controller applications[30]. However, phase segregation is a critical issue in these alloys. If Ge atoms segregate and form small clusters, then the remaining switching component reverts to stoichiometric GST phases, e.g., $Ge_2Sb_2Te_5$, $Ge_1Sb_2Te_4$, or others[31], and the amorphous-phase stability in subsequent switching processes would therefore be seriously weakened. A survey of the relevant PCMs in the ternary system, including an indication of their application frontiers, is given in Fig. 1. The measured T_x values, indicated by color coding in that figure, are taken from refs [28,32–34].

Despite the practical importance of Ge-rich GST alloys, the atomic origin of the enhanced amorphous stability remains elusive, which has precluded the development of materials optimization guidelines (as have been successful for SST and $TiTe_2/Sb_2Te_3$ heterostructure). Therefore, in the present work, we carry out density functional theory (DFT) based ab initio molecular dynamics (AIMD) simulations and orbital-based bonding analyses to assess the structural features and bonding nature of amorphous Ge-rich GST phases, ranging in composition from $Ge_2Sb_1Te_2$ up to $Ge_7Sb_1Te_2$. In comparison with pure amorphous Ge, GeTe, and several stoichiometric GST alloys, the role of excess Ge content in improving the amorphous stability is elucidated. Analyses of medium-range order and kernel similarity to crystalline phases through the smooth overlap of atomic positions (SOAP) method[19,35,36] provide insight into the structural nature of the increasingly Ge-rich phases. Our computations allow us to suggest a threshold value of Ge concentration for viable Ge-rich GST alloys, marked by the green dashed circle in Fig. 1, and a materials design strategy for high-performance embedded phase-change memory applications.

RESULTS

Modeling Ge-rich phase-change materials

Structural models of amorphous Ge, GeTe, and multiple GST alloys of different stoichiometric compositions were generated following a melt–quench protocol[37] (see "Methods"). For each composition, three independent runs were performed for data collection. All models, including the stoichiometric compositions $Ge_2Sb_2Te_5$, $Ge_1Sb_2Te_4$, $Ge_1Sb_4Te_7$, $Ge_3Sb_2Te_6$, and $Ge_8Sb_2Te_{11}$, were generated in cubic boxes with 189–210 atoms, corresponding to a $3 \times 3 \times 3$ supercell of the recrystallized cubic rocksalt-type phase[38–40]. The number of atoms in some models was slightly increased to account for the exact stoichiometry, e.g., $Ge_2Sb_2Te_5$ with 44 Ge, 44 Sb, and 110 Te atoms. Keeping the number of Sb and Te atoms fixed to the value found in the $Ge_1Sb_2Te_4$ model (that is, 54 Sb and 108 Te atoms, respectively), the number of Ge atoms was increased to describe amorphous $Ge_2Sb_1Te_2$ (270 atoms), $Ge_3Sb_1Te_2$ (324 atoms), $Ge_4Sb_1Te_2$ (378 atoms), $Ge_5Sb_1Te_2$ (432 atoms), $Ge_6Sb_1Te_2$ (486 atoms), and $Ge_7Sb_1Te_2$ (540 atoms). The size of the simulation box was adjusted several times during quenching to reduce the internal pressure for all models. Figure 2a shows the atomic structures of four amorphous alloys with increasing Ge content. The theoretical number density value is gradually increased with higher Ge content: 0.0278, 0.0310, 0.0327, and 0.0358 Å^{-3} for amorphous $Ge_2Sb_2Te_5$, $Ge_2Sb_1Te_2$, $Ge_4Sb_1Te_2$, and $Ge_7Sb_1Te_2$, respectively, approaching that computed for elemental amorphous Ge with the same melt–quench protocol and high cooling rate, viz. 0.0430 Å^{-3} (Supplementary Figure 1). The radial distribution functions (RDFs) of these Ge-rich phases at 300 K are shown in Supplementary Figure 2. As the Ge concentration increases, the peaks of the Ge–Ge and Ge–Sb RDFs become more pronounced. However, even in amorphous $Ge_7Sb_1Te_2$, Ge–Te bonds still remain a major structural feature, whereas no Te–Te pair is found at a small interatomic distance. Visual inspection also does not suggest substantial de-mixing: all generated amorphous models, including the Ge-rich ones, still represent homogeneous phases (Fig. 2a). The spatial homogeneity of stoichiometric and Ge-rich GST amorphous models is further quantified by SOAP analyses in Supplementary Figure 3. Thorough X-ray or electron diffraction based measurements[41–47] are anticipated to assess the geometrical configurations of these amorphous Ge-rich GST alloys.

Chemical bonding analyses using the crystal orbital overlap population (COOP) method and a projection onto local, atom-centered orbitals[48–50] were performed for relaxed structural snapshots of the Ge-rich amorphous phases, following an approach we have previously proposed for amorphous GeTe[46,47]. The COOP curves show no strong antibonding interaction at the Fermi level for both amorphous $Ge_2Sb_2Te_5$ and $Ge_2Sb_1Te_2$ (Supplementary Figure 4), indicating reasonable chemical stability of the amorphous models. For a specific pair of atoms A and B, the strength of the covalent bond between them can be estimated by calculating the bond population, B_{AB}, by integrating its projected COOP up to the Fermi level, E_F. As shown in Supplementary Figure 2, all interatomic pairs show positive bond populations at a small interatomic distance below 3 Å, while as the interatomic distance further increases, a crossover from stabilizing bonding interaction to destabilizing antibonding interaction appears for heteropolar Ge–Te and Sb–Te bonds, and (quasi-)homopolar Ge–Ge, Ge–Sb, and Sb–Sb bonds. Te–Te bonds instead show mostly antibonding interaction at larger interatomic distances. Despite the difference in composition, all the four amorphous alloys show a consistent set of crossover from bonding to antibonding interactions (positive to negative B_{AB}), defining the bond cutoffs as Ge–Ge: 3.06 Å, Ge–Sb: 3.19 Å, Sb–Sb: 3.18 Å, Ge–Te: 3.15 Å, and Sb–Te: 3.22 Å, respectively (see Supplementary Figure 2 for details).

These BWDF-determined bond-length cutoffs now enabled a series of geometrical analyses to understand the structural

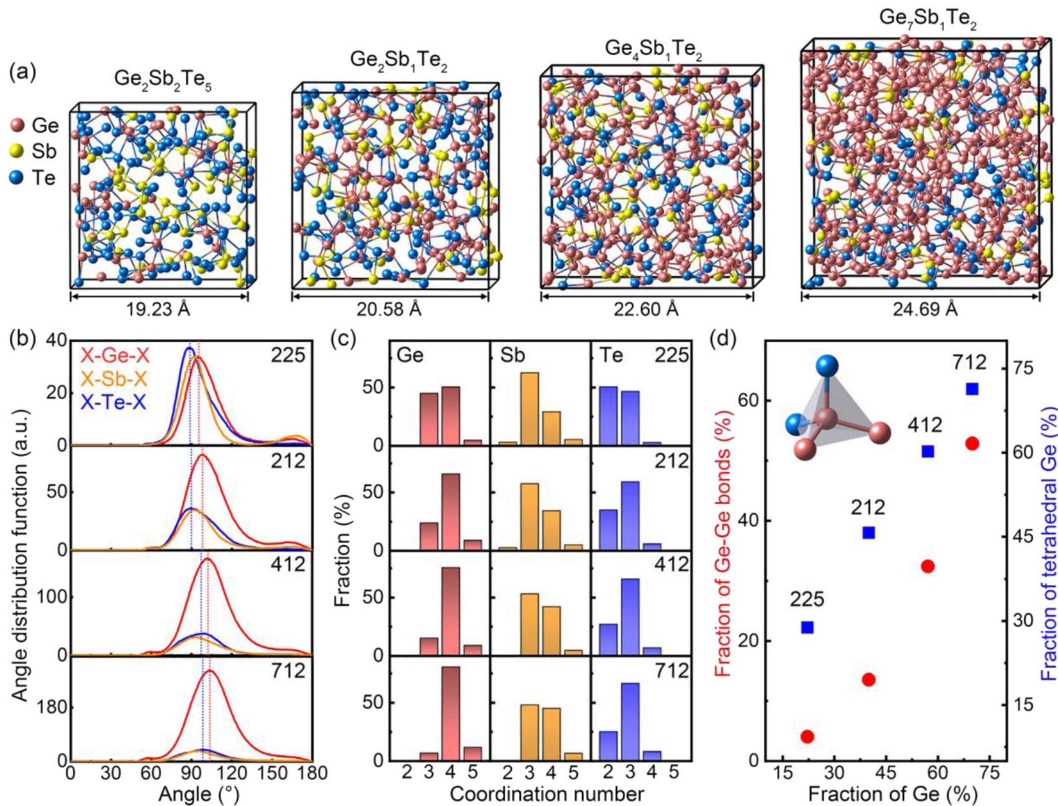

Fig. 2 Structural features of amorphous GST models. a Atomic structures of amorphous $Ge_2Sb_2Te_5$, $Ge_2Sb_1Te_2$, $Ge_4Sb_1Te_2$, and $Ge_7Sb_1Te_2$ generated via melt–quench AIMD simulations. Ge, Sb, and Te atoms are rendered as red, yellow, and blue spheres, respectively. **b** The angular distribution functions (ADF), **c** the distribution of the coordination number (CN) and **d** the fraction of homopolar Ge–Ge bonds and tetrahedral Ge motifs for the four amorphous GST models. The inset in **d** shows a typical tetrahedral Ge motif with two homopolar Ge–Ge bonds.

properties of the Ge-rich amorphous phases. Figure 2b shows the angular distribution functions (ADFs) collected for each elemental species. A strong shift of the ADF peak for Ge-centered motifs towards 109° is observed upon moving from amorphous $Ge_2Sb_2Te_5$ to $Ge_7Sb_1Te_2$, while the ADF for Sb-centered motifs remains around 90°. These trends indicate that the Sb atoms are mostly in defective octahedral configurations even in amorphous $Ge_7Sb_1Te_2$, while the Ge atoms become mostly tetrahedrally bonded in amorphous Ge-rich GST alloys, resembling more closely the amorphous Ge. The moderate shift toward higher angles in the Te-ADF is due to more Te atoms becoming associated with Ge atoms in tetrahedral coordination in amorphous Ge-rich GST. This observation is further supported by the distribution of coordination numbers (CNs) shown in Fig. 2c, where a major change is found in Ge-centered motifs from a mixture of three- and fourfold motifs in amorphous $Ge_2Sb_2Te_5$ to mostly fourfold ones in the other three Ge-rich GST models. Sb and Te atoms also tend to have more neighboring atoms in the latter three amorphous models. We calculated the bond order parameter $q = 1 - \frac{3}{8}\sum_{B>A}\left(\frac{1}{3} + \cos\theta_{ABC}\right)^2$ between three neighboring atoms A, B, and C for all Ge atoms, where θ_{ABC} refers to the bond angle between bond A–B and bond B–C[51]. A gradual increase in tetrahedral concentration (defined as $q > 0.8$) from ~30 to ~70% from $Ge_2Sb_2Te_5$ to $Ge_7Sb_1Te_2$ was found (Fig. 2d). As expected, this increase in the fraction of tetrahedral Ge is strongly correlated with the occurrence of homopolar Ge–Ge bonds, which were shown to be the primary source of stabilization for tetrahedral motifs in amorphous GeTe[52].

Next, we assess the medium-range order of the amorphous models through primitive-ring statistics (Fig. 3). For the stoichiometric GST alloys with comparable fraction of GeTe and Sb_2Te_3 content, the fourfold rings, in particular ABAB rings (A = Ge or Sb, B = Te), are the dominant structural fragment. Figure 3a shows the case of amorphous $Ge_2Sb_2Te_5$, with almost 9 out of 10 fourfold rings showing ABAB alternation[42,51,53,54]. As the GeTe content increases, the fraction of fivefold rings becomes comparable to that of fourfold ones in amorphous $Ge_8Sb_2Te_{11}$ and GeTe (Fig. 3b, c). Within the fourfold rings, ABAB alternation still dominates with a share of ~90% (Table 1)[54–56]. The abundant presence of ABAB rings is regarded as the precursor for rapid crystallization at elevated temperatures[2,42,51,53,54]. However, the rings pattern changes drastically in amorphous Ge-rich GST alloys. As shown in Fig. 3d–f, fivefold rings are the dominant structural fragment identified in our simulations. The fraction of fourfold rings as well as ABAB rings reduces sharply in these Ge-rich GST alloys (Table 1) due to the much more abundant homopolar Ge–Ge bonds (Fig. 2d). In amorphous $Ge_4Sb_1Te_2$ and $Ge_7Sb_1Te_2$, a non-negligible fraction of threefold Ge–Ge–Ge rings is also observed, at variance with the Ge-poorer phases, indicating a possible local instability associated with large ring strain. There is also a gradual increase in sixfold rings in Ge-rich GST moving towards elemental Ge, as the sixfold rings are the most abundant ring pattern in amorphous Ge (Supplementary Figure 5) as well as in the homologous amorphous silicon (see, e.g., ref. [57] and references therein). We note that fivefold ring dominated structures were also observed in Sb-rich PCMs, for which the nucleation rate is much lower than that of stoichiometric GST[58–61].

SOAP similarity analysis

Clearly, Ge atoms tend to cluster in amorphous $Ge_7Sb_1Te_2$, reducing the abundance of those structural patterns that are essential for rapid nucleation in the established GST alloys:

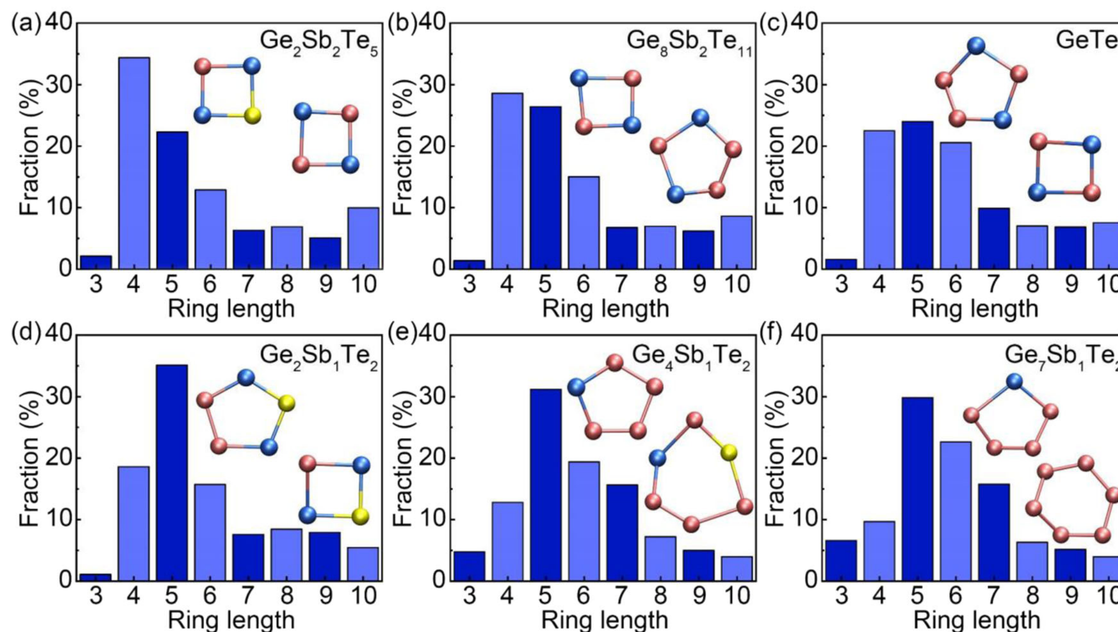

Fig. 3 Primitive rings statistics. The distribution of primitive rings for six amorphous alloys, including stoichiometric GST **a** $Ge_2Sb_2Te_5$ and **b** $Ge_8Sb_2Te_{11}$, **c** GeTe, and off-stoichiometric GST **d** $Ge_2Sb_1Te_2$, **e** $Ge_4Sb_1Te_2$, and **f** $Ge_7Sb_1Te_2$. The insets show typical ring fragments in respective amorphous models. Ge, Sb, and Te atoms are shown in red, yellow, and blue, respectively.

Table 1. The statistics of ABAB rings for the six alloys characterized in Fig. 3.

ABAB/4-fold rings (%)	$Ge_2Sb_2Te_5$	$Ge_8Sb_2Te_{11}$	GeTe	$Ge_2Sb_1Te_2$	$Ge_4Sb_1Te_2$	$Ge_7Sb_1Te_2$
Ge–Te–Ge–Te	26.9	62.6	90.0	41.3	23.0	9.7
Sb–Te–Sb–Te	13.1	2.0	/	1.1	0.0	0.0
Ge–Te–Sb–Te	48.1	23.1	/	10.0	1.7	0.0
Sum	88.1	87.7	90.0	52.4	24.7	9.7

The fractional values are obtained by dividing the number of ABAB rings by the total number of fourfold rings. The remaining fourfold rings (e.g., about 12% in $Ge_2Sb_2Te_5$) do not have ABAB composition but include homopolar contacts.

namely, the predominance of defective octahedral motifs and ABAB rings. To quantify the local structural similarity with respect to elemental amorphous Ge (a-Ge), we use the SOAP formalism. As shown in the inset of Fig. 4, a set of Gaussian functions is placed on each atomic position inside a sphere with a cutoff r_c. The SOAP kernel value is then obtained via an expansion of this neighbor density in a series of basis functions, as detailed in ref. [35]. The result is a value ranging from 0 to 1, characterizing the degree of structural similarity between two given atomic environments. We consider both the nearest-neighbor (NN) and the next-nearest-neighbor (NNN) environments in the amorphous models[57]: note that we use cut-off values larger than the BWDF bond cutoffs to include more aspects of the atomic structure (here, $r_c = 3.5$ and 5.5 Å for NN and NNN). Further details can be found in the "Methods" or in refs [19,35,36].

We calculated the SOAP kernel values for all simulated amorphous GST models with respect to a rapidly quenched a-Ge structure (obtained using the same quenching approach as our GST models, for full consistency), as shown in Fig. 4. Moving along the stoichiometric GeTe–Sb_2Te_3 quasi-binary line towards amorphous GeTe (squares), a nearly monotonous increase is observed in both NN (blue), and NNN (red) SOAP similarity to a-Ge. In contrast, the amorphous Ge-rich GST alloys (circles) clearly deviate from this behavior as soon as one leaves the GeTe–Sb_2Te_3 quasi-binary line (i.e., the 'usual' GST materials), emphasizing how a change in chemical composition is associated with a change in local structure. A sharp increase, in particular, in the NNN SOAP similarity to a-Ge is found between $Ge_2Sb_1Te_2$ and $Ge_5Sb_1Te_2$. A structural snapshot, together with RDF and bond population analyses, of rapidly quenched amorphous Ge is shown in Supplementary Figure 1. For $Ge_7Sb_1Te_2$, the overall structural similarity to a-Ge is rather high, as expected, at least up to the chosen NNN cutoff. Nevertheless, this phase is still very different from the strongly segregated phase observed in experiments under high annealing temperatures, where stoichiometric GST grains and nanoscale elemental Ge clusters were found[31].

Energetics of phase separation

To probe the compositional boundary of phase separation, we compute the energy difference E_{diff} of the amorphous phases in analogy to the formation energy of crystalline alloys. Given that all the Ge-rich GST models were constructed by adding more Ge atoms into the $Ge_1Sb_2Te_4$ model, we calculated E_{diff} by subtracting the total energy of amorphous Ge-rich models with respect to $Ge_1Sb_2Te_4$ and Ge in the amorphous form, $E_{diff} = E_{GeRich} - E_{124} - N_{Ge}E_{Ge}$, as shown in Fig. 5a. For each amorphous alloy, three independent melt-quenched models are considered for average. The large error bars come mostly from the calculations of amorphous $Ge_1Sb_2Te_4$ and amorphous Ge, due to their smaller model size. Nevertheless, a clear crossover from negative values to positive ones is identified in E_{diff} between '312' and '412'. As sketched in Fig. 5b, the negative E_{diff}

values indicate that the Ge-rich GST is still energetically more favorable in the homogeneous amorphous form, while the positive values would suggest that the system becomes energetically more favorable in the form of stoichiometric GST and amorphous Ge. This composition threshold determined by energetics may be compared with the SOAP structural analyses, where a rapid increase in structural similarity with respect to elemental a-Ge is observed between the '212' and '512' stoichiometric compositions.

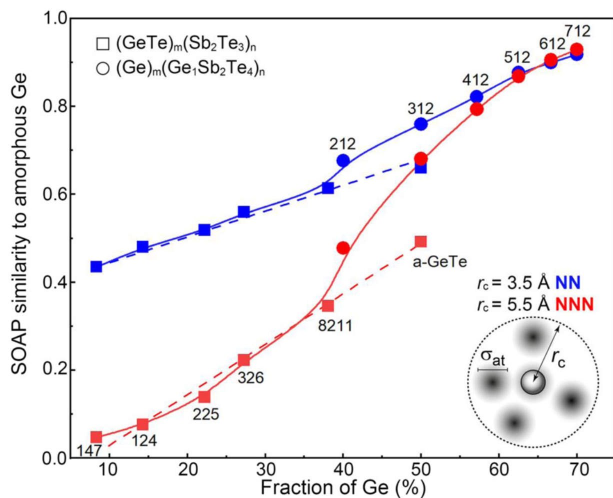

Fig. 4 SOAP analysis. Structural similarity of the various amorphous phases to amorphous Ge, as quantified by the SOAP kernel (see "Methods"). The normalized SOAP similarity represents the global similarity of all Ge-centered motifs in amorphous stoichiometric GST and GeTe (squares) and Ge-rich GST (circles), with respect to amorphous Ge (quenched using the same protocol); a value of 1.0 indicates indistinguishable environments (up to a given cut-off radius). More specifically, for a given atom in one amorphous GST or GeTe sample, a SOAP similarity value with respect to one atom in one amorphous Ge model is calculated, and then averaged over all atomic environments in three independent amorphous Ge models. The kernel similarity is then averaged over all atomic environments in a given amorphous sample of GST or GeTe, and subsequently, over three independent amorphous samples. The lower inset sketches the smoothed atomic neighbor density that is used as the basis for SOAP analysis. The radial cutoffs are 3.5 Å for short-range (NN—nearest neighbor, blue) and 5.5 Å for medium-range (NNN—next nearest neighbor, red) similarity to amorphous Ge.

Device degradation and materials design strategy

For embedded memories in automobiles, the stored digital information has to endure very high environmental temperatures, e.g., above 250 °C. It is also crucial that phase separation is avoided during cycling to maintain the high stability of the homogeneous amorphous phase. Once phase separation occurs, elemental Ge clusters could be gradually crystallized during the RESET operation, during which the memory cell is heated above the melting temperature T_M of GST ~650 °C, as the crystallization temperature of amorphous Ge is between 400 and 650 °C (this large variation is due to different experimental conditions, as discussed in ref. [62]). For subsequent programming cycles, it would not likely be possible to switch the crystalline Ge clusters any more, due to the very high melting point of Ge crystals above 938 °C. Therefore, the remainder, stoichiometric 'regular' GST phases, would act as programmable medium (according to a formal reaction of, e.g., 2 $Ge_2Sb_1Te_2 \rightarrow 3\ Ge + Ge_1Sb_2Te_4$), but these phases have much lower T_x (~150 °C). Therefore, if Ge precipitation occurred, the device would be expected to fail for further embedded memory use.

As shown in Fig. 1, T_x increases from Sb_2Te_3 (85 °C) to GeTe (192 °C) along the stoichiometric tie-line, while all the off-stoichiometric GST show a relatively high T_x. Starting from $Ge_2Sb_1Te_2$, T_x is increased from ~250 to ~310 °C at a composition close to $Ge_5Sb_1Te_2$. The increase in T_x for either the stoichiometric or Ge-rich GST phases can be understood as being due to the increase in structural similarity with respect to amorphous Ge. It is noted that despite the higher Ge concentration in GeTe (50%) than in $Ge_2Sb_1Te_2$ (40%), the amorphous structure of the latter resembles amorphous Ge more closely than that of the former (Fig. 4). Accordingly, the corresponding T_x of GeTe thin film is lower than that of $Ge_2Sb_1Te_2$. It is also important to note that all T_x values shown in Fig. 5b were measured using as-deposited amorphous thin films, corresponding only to one-time crystallization under isothermal heating condition. While for practical applications in devices, repeated programming through melt-quenched amorphization and subsequent crystallization would result in a very strong tendency towards phase separation, if the Ge concentration exceeded ~50%. A very recent experimental work on crystallization kinetics of Ge-rich GST provides strong support for this theoretical prediction[63]. In ref. [63], the total Ge concentration of the as-deposited Ge-rich GST thin film was over 50% ($Ge_2Sb_2Te_5$ with 45% excess Ge), and many crystalline Ge clusters precipitated upon annealing at 400 °C, which were no

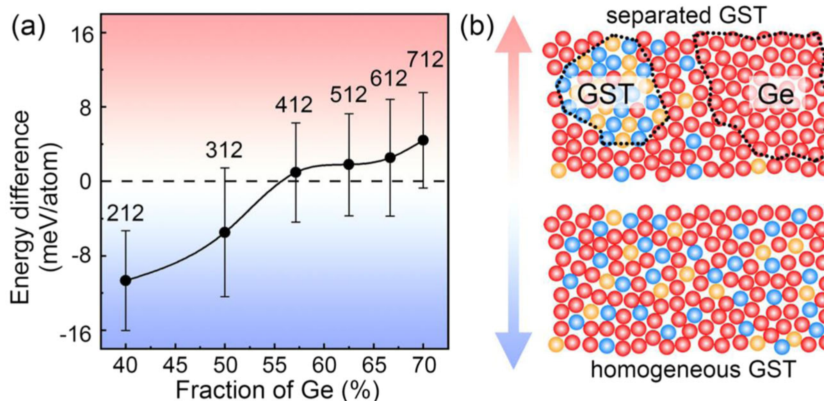

Fig. 5 Energy analysis of the phase segregation. **a** The energy difference E_{diff} of amorphous Ge-rich GST with respect to amorphous $Ge_1Sb_2Te_4$ and amorphous Ge as a function of the Ge concentration, as defined in the text. Each data point is averaged over three samples of a specific Ge-rich GST alloy, three samples of amorphous $Ge_1Sb_2Te_4$ and three samples of amorphous Ge. The large error bars are mostly contributed by the energy fluctuations of amorphous $Ge_1Sb_2Te_4$ and amorphous Ge models, due to their limited system size. **b** The sketches of separated GST phase and homogeneous GST phase. Positive E_{diff} values reveal an intrinsic tendency toward phase separation into amorphous $Ge_1Sb_2Te_4$ and amorphous Ge, while negative E_{diff} values indicate that the amorphous models are energetically favorable in the homogeneous phase.

longer switchable in the subsequent melt-quenching process by laser irradiation. Depending on the irradiation conditions, the residual excess Ge in the programmable area was estimated to be ~15–20%. Although not specified, the initial T_x of the as-deposited Ge-rich GST thin film is derived to be above 380 °C, as compared to the compositions reported in refs. [28–31], and the T_x drops to 245–275 °C after partial segregation of excess Ge[63].

Therefore, for storage-oriented applications that would require very high working temperatures above, e.g., 300 °C, we suggest further materials engineering starting from $Ge_3Sb_1Te_2$ (T_x ~ 275 °C), $Ge_2Sb_1Te_2$ (T_x ~ 250 °C), or other GST compositions with smaller Ge concentration, as marked by the green dashed circle in Fig. 1. Enhanced amorphous stability might be achieved, for instance, via doping with impurities like C or N[25–27]. For example, N atoms were shown to bond mostly with Ge atoms in amorphous $Ge_2Sb_2Te_5$[64]. This bonding pattern is expected to reduce the tendency of elemental Ge segregation. Alternatively, the amorphous-phase stability of Ge-rich GST alloys could potentially be enhanced by reducing the film thickness to a few nanometers. Indeed, it was shown that elemental Sb, which normally crystallizes spontaneously at room temperature, could be stabilized in either melt-quenched[65] or as-deposited[66] amorphous forms for several tens of hours by reducing the system size to ~3–4 nm thin films. This approach employs nanosized confinement effects brought about by the surrounding materials[67], with no need to change the chemical composition of the active PCM.

Future work on the crystalline phase is anticipated for a better understanding of the SET process of Ge-rich GST devices. It is well known that the GST alloys along the $GeTe–Sb_2Te_3$ pseudo-binary line tend to crystallize into a cubic rocksalt structure with a high amount of atomic vacancies[38–40]. Yet, for the Ge-rich GST devices used in practice[28–31], the Ge concentration ranges from ~35 to ~45%, exceeding the maximum of a cubic structure by full occupation of the vacant sites, i.e., $Ge_1Sb_2Te_4 \rightarrow Ge_1Sb_1Te_2$ (25%) or $Ge_2Sb_2Te_5 \rightarrow Ge_3Sb_2Te_5$ (30%). In refs. [29,31], the recrystallized Ge-rich GST thin films upon long-term thermal annealing, e.g., 30 min at 400 °C and above, show a clear separation into GST and Ge crystals. However, this crystalline state may be different from what obtained in devices via rapid electrical pulses of tens to hundreds of ns. Because an effective reduction, rather than an increase, in RESET current is consistently observed in Ge-rich GST devices[28,29,31], indicating weaker stability of the crystalline state. In contrast, crystalline Ge with a much higher stability (T_M = 938 °C) would require more thermal energy to melt down. As shown in ref. [63], further phase segregation upon crystallization at 300 °C was not observed for the medium-level Ge-rich GST areas ($Ge_2Sb_2Te_5$ with 15–20% excess Ge), indicating the formation of a different crystalline structure other than the well-studied cubic rocksalt phase. Hence, more research efforts, for example, cross-sectional transmission electron microscopy (TEM) characterizations of the SET state of Ge-rich GST devices, are needed for better clarity.

DISCUSSION

We performed a comprehensive ab initio molecular dynamics study of Ge-rich GST alloys for embedded phase-change memory applications. The essential bonding patterns for rapid nucleation of stoichiometric GST, including octahedral motifs and ABAB rings, are strongly affected by the presence of additional Ge content off the $GeTe–Sb_2Te_3$ pseudo-binary line. With the increase in Ge–Ge homopolar bonds, the concentration of tetrahedral motifs is increased from ~30% in amorphous $Ge_2Sb_2Te_5$ to ~70% in amorphous $Ge_7Sb_1Te_2$. SOAP kernel similarity analyses show a gradual increase in structural similarity of amorphous GST with respect to amorphous Ge along both the $GeTe–Sb_2Te_3$ pseudo-binary line and the $Ge_2Sb_1Te_2$–Ge tie-line, but with a distinctly different trend in both materials classes, which is easily visualized using the kernel similarity approach. The increased structural similarity to amorphous Ge is consistent with the rise in crystallization temperature of amorphous GST, as amorphous Ge has a high T_x above 400 °C. However, our energetic considerations suggest an optimal compositional pool in the Ge–Sb–Te ternary diagram around $Ge_2Sb_1Te_2$ and $Ge_3Sb_1Te_2$, as we identify a compositional threshold of ~50% Ge concentration, distinguishing homogenous GST alloys from heterogeneous ones with a strong tendency towards phase separation. Based on these ab initio simulations, we propose a materials design strategy for high-performance embedded phase-change memories with balanced speed and stability as well as potentially good cycling capability.

METHODS

DFT computations

To generate amorphous structural models, density functional theory (DFT) based ab initio molecular dynamics (AIMD) simulations were performed using the second-generation Car–Parrinello scheme in the canonical ensemble (NVT) with a stochastic Langevin thermostat[68]. The size of the simulation box was adjusted five times to reduce the internal stress during quenching. The time step was 2 fs, and the Γ point was used to sample the Brillouin zone of all models. All AIMD simulations were performed using the CP2K package[69], employing a mixed scheme of plane waves and Gaussian-type basis sets. Plane waves with a cutoff of 300 Ry were used to calculate the charge density. The Kohn–Sham orbitals were expanded in Gaussian basis sets with triple-zeta plus polarization quality. The Goedecker pseudopotentials[70] and the Perdew–Burke–Ernzerhof (PBE) functional[71] were used. The obtained amorphous structures were further relaxed using the Vienna Ab initio Simulation Package (VASP)[72] with the projector augmented-wave (PAW) pseudopotentials[73] and the PBE functional. The Kohn–Sham states were expanded in plane waves with an energy cutoff of 500 eV. After the self-consistent calculations, the VASP wave functions were then projected onto an auxiliary basis of localized, atom-centered orbitals for crystal orbital overlap population (COOP) analysis, as implemented in the local orbital basis suite towards electronic-structure reconstruction (LOBSTER) code[48–50].

SOAP structural analysis

The SOAP formalism has been applied in structural analyses of a variety of materials[74], including alloyed Sb_2Te_3[19], and in the fitting of machine learning interatomic potentials (ref. [75] and references therein) including one for liquid, amorphous, and crystalline $Ge_2Sb_2Te_5$[76]. The SOAP similarity measure is based on the local atomic density, smoothed by Gaussian functions and expanded on the basis of radial functions and spherical harmonics. Here we use the DScribe[77] implementation of SOAP, with $n_{max} = 14$ and $l_{max} = 9$ as convergence parameters. Similar to ref. [57], different σ_{at} values of 0.3 and 0.6 Å are used for NN (r_c = 3.5 Å) and NNN (r_c = 5.5 Å) environments, respectively, controlling the 'fuzziness' of the atomic neighbor densities.

DATA AVAILABILITY

The data that support the findings of this study are available from the corresponding author, Professor Wei Zhang (email: wzhang0@mail.xjtu.edu.cn), upon reasonable request.

Received: 2 November 2020; Accepted: 11 January 2021;
Published online: 08 February 2021

REFERENCES

1. Wuttig, M. & Yamada, N. Phase-change materials for rewriteable data storage. *Nat. Mater.* **6**, 824–832 (2007).
2. Zhang, W., Mazzarello, R., Wuttig, M. & Ma, E. Designing crystallization in phase-change materials for universal memory and neuro-inspired computing. *Nat. Rev. Mater.* **4**, 150–168 (2019).
3. Wang, Z. et al. Resistive switching materials for information processing. *Nat. Rev. Mater.* **5**, 173–195 (2020).
4. Yamada, N., Ohno, E., Nishiuchi, K., Akahira, N. & Takao, M. Rapid-phase transitions of GeTe-Sb_2Te_3 pseudobinary amorphous thin films for an optical disk memory. *J. Appl. Phys.* **69**, 2849–2856 (1991).

5. Loke, D. et al. Breaking the speed limits of phase-change memory. *Science* **336**, 1566–1569 (2012).
6. Fong, S. W., Neumann, C. M. & Wong, H.-S. P. Phase-change memory—towards a storage-class memory. *IEEE Trans. Electron. Dev.* **64**, 4374–4385 (2017).
7. Ambrogio, S. et al. Equivalent-accuracy accelerated neural network training using analogue memory. *Nature* **558**, 60–67 (2018).
8. Zhang, Y. et al. Brain-inspired computing with memristors: challenges in devices, circuits, and systems. *Appl. Phys. Rev.* **7**, 011308 (2020).
9. Wang, W. H., Chung, L. C. & Kuo, C. T. Effects of the Sb_2Te_3 crystallization-induced layer on crystallization behaviors and properties of phase change optical disk. *Surf. Coat. Technol.* **177–178**, 795–799 (2004).
10. Rao, F. et al. Reducing the stochasticity of crystal nucleation to enable sub-nanosecond memory writing. *Science* **358**, 1423–1427 (2017).
11. Chen, B. et al. Kinetics features conducive to cache-type nonvolatile phase-change memory. *Chem. Mater.* **31**, 8794–8800 (2019).
12. Ding, K. et al. Recipe for ultrafast and persistent phase-change memory materials. *NPG Asia Mater.* **12**, 63 (2020).
13. Hu, S., Liu, B., Li, Z., Zhou, J. & Sun, Z. Identifying optimal dopants for Sb_2Te_3 phase-change material by high-throughput ab initio calculations with experiments. *Comput. Mater. Sci.* **165**, 51–58 (2019).
14. Qiao, C. et al. Local structure origin of ultrafast crystallization driven by high-fidelity octahedral clusters in amorphous $Sc_{0.2}Sb_2Te_3$. *Appl. Phys. Lett.* **114**, 071901 (2019).
15. Wang, X.-P. et al. Time-dependent density-functional theory molecular-dynamics study on amorphization of Sc-Sb-Te alloy under optical excitation. *npj Comput. Mater.* **6**, 31 (2020).
16. Li, Z., Si, C., Zhou, J., Xu, H. & Sun, Z. Yttrium-doped Sb_2Te_3: a promising material for phase-change memory. *ACS Appl. Mater. Interfaces* **8**, 26126–26134 (2016).
17. Liu, B. et al. Y-doped Sb_2Te_3 phase-change materials: toward a universal memory. *ACS Appl. Mater. Interfaces* **12**, 20672–20679 (2020).
18. Hu, S., Xiao, J., Zhou, J., Elliott, S. R. & Sun, Z. Synergy effect of co-doping Sc and Y in Sb_2Te_3 for phase-change memory. *J. Mater. Chem. C.* **8**, 6672–6679 (2020).
19. Zhou, Y. et al. Bonding similarities and differences between Y–Sb–Te and Sc–Sb–Te phase-change memory materials. *J. Mater. Chem. C.* **8**, 3646–3654 (2020).
20. Ielmini, D., Lacaita, A. L. & Mantegazza, D. Recovery and drift dynamics of resistance and threshold voltages in phase-change memories. *IEEE Trans. Electron. Dev.* **54**, 308–315 (2007).
21. Ding, K. et al. Phase-change heterostructure enables ultralow noise and drift for memory operation. *Science* **366**, 210–215 (2019).
22. Gholipour, B. The promise of phase-change materials. *Science* **366**, 186–187 (2019).
23. Cappelletti, P. et al. Phase change memory for automotive grade embedded NVM applications. *J. Phys. D: Appl. Phys.* **53**, 193002 (2020).
24. Li, X. et al. Enhancing performances of phase change memory for embedded applications. *Phys. Status Solidi RRL* **13**, 1800558 (2019).
25. Horii, H. et al. A novel cell technology using N-doped GeSbTe films for phase change RAM. *VLSI Tech. Dig.* 17–18 (2003).
26. Shelby, R. M. & Raoux, S. Crystallization dynamics of nitrogen-doped $Ge_2Sb_2Te_5$. *J. Appl. Phys.* **105**, 104902 (2009).
27. Song, Z. T. et al. High endurance phase change memory chip implemented based on carbon-doped $Ge_2Sb_2Te_5$ in 40 nm node for embedded application. *IEDM Tech. Dig.* 27.5.1–27.5.4 (2018).
28. Cheng, H. Y. et al. A high performance phase change memory with fast switching speed and high temperature retention by engineering the $Ge_xSb_yTe_z$ phase change material. *IEDM Tech. Dig.* 3.4.1–3.4.4 (2011).
29. Navarro, G. et al. Trade-off between SET and data retention performance thanks to innovative materials for phase-change memory. *IEDM Tech. Dig*. 21.5.1–21.5.4 (2013).
30. Arnaud, F. et al. Truly innovative 28 nm FDSOI technology for automotive micro-controller applications embedding 16 MB phase change memory. *IEDM Tech. Dig.* 18.4.1–18.4.4 (2018).
31. Agati, M., Vallet, M., Joulie, S., Benoit, D. & Claverie, A. Chemical phase segregation during the crystallization of Ge-rich GeSbTe alloys. *J. Mater. Chem. C.* **7**, 8720–8729 (2019).
32. Siegrist, T. et al. Disorder-induced localization in crystalline phase-change materials. *Nat. Mater.* **10**, 202–208 (2011).
33. Jost, P. et al. Disorder-induced localization in crystalline pseudo-binary GeTe-Sb_2Te_3 alloys between $Ge_3Sb_2Te_6$ and GeTe. *Adv. Funct. Mater.* **25**, 6399–6406 (2015).
34. Bouska, M. et al. Pulsed laser deposited GeTe-rich GeTe-Sb_2Te_3 thin films. *Sci. Rep.* **6**, 26552 (2016).
35. Bartók, A. P., Kondor, R. & Csányi, G. On representing chemical environments. *Phys. Rev. B* **87**, 184115 (2013).
36. De, S., Bartók, A. P., Csányi, G. & Ceriotti, M. Comparing molecules and solids across structural and alchemical space. *Phys. Chem. Chem. Phys.* **18**, 13754–13769 (2016).
37. Zhang, W. et al. Density functional theory guided advances in phase-change materials and memories. *MRS Bull.* **40**, 856–865 (2015).
38. Yamada, N. & Matsunaga, T. Structure of laser-crystallized $Ge_2Sb_{2+x}Te_5$ sputtered thin films for use in optical memory. *J. Appl. Phys.* **88**, 7020–7028 (2000).
39. Ross, U., Lotnyk, A., Thelander, E. & Rauschenbach, B. Direct imaging of crystal structure and defects in metastable $Ge_2Sb_2Te_5$ by quantitative aberration-corrected scanning transmission electron microscopy. *Appl. Phys. Lett.* **104**, 121904 (2014).
40. Zhang, B. et al. Element-resolved atomic structure imaging of rocksalt $Ge_2Sb_2Te_5$ phase-change material. *Appl. Phys. Lett.* **108**, 191902 (2016).
41. Kolobov, A. V. et al. Understanding the phase-change mechanism of rewritable optical media. *Nat. Mater.* **3**, 703–708 (2004).
42. Kohara, S. et al. Structural basis for the fast phase change of $Ge_2Sb_2Te_5$: Ring statistics analogy between the crystal and amorphous states. *Appl. Phys. Lett.* **89**, 201910 (2006).
43. Zhang, W. et al. How fragility makes phase-change data storage robust: insights from ab initio simulations. *Sci. Rep.* **4**, 6529 (2014).
44. Kooi, B. J., Groot, W. M. G. & Hosson, J. T. M. D. In situ transmission electron microscopy study of the crystallization of $Ge_2Sb_2Te_5$. *J. Appl. Phys.* **95**, 924 (2004).
45. Lotnyk, A. et al. Real-space imaging of atomic arrangement and vacancy layers ordering in laser crystallised $Ge_2Sb_2Te_5$ phase change thin films. *Acta Mater.* **105**, 1–8 (2016).
46. Hirata, A., Ichitsubo, T., Guan, P. F., Fujita, T. & Chen, M. W. Distortion of local atomic structures in amorphous Ge-Sb-Te phase change materials. *Phys. Rev. Lett.* **120**, 205502 (2018).
47. Zhang, W. & Ma, E. Unveiling the structural origin to control resistance drift in phase-change memory materials. *Mater. Today* **41**, 156–176 (2020).
48. Hughbanks, T. & Hoffmann, R. Chains of trans-edge-sharing molybdenum octahedra: metal-metal bonding in extended systems. *J. Am. Chem. Soc.* **105**, 3528–3537 (1983).
49. Maintz, S., Deringer, V. L., Tchougreeff, A. L. & Dronskowski, R. LOBSTER: a tool to extract chemical bonding from plane-wave based DFT. *J. Comput. Chem.* **37**, 1030–1035 (2016).
50. Nelson, R. et al. LOBSTER: Local orbital projections, atomic charges, and chemical-bonding analysis from projector-augmented-wave-based density-functional theory. *J. Comput. Chem.* **41**, 1931–1940 (2020).
51. Caravati, S., Bernasconi, M., Kühne, T. D., Krack, M. & Parrinello, M. Coexistence of tetrahedral- and octahedral-like sites in amorphous phase change materials. *Appl. Phys. Lett.* **91**, 171906 (2007).
52. Deringer, V. L. et al. Bonding nature of local structural motifs in amorphous GeTe. *Angew. Chem. Int. Ed.* **53**, 10817–10820 (2014).
53. Hegedüs, J. & Elliott, S. R. Microscopic origin of the fast crystallization ability of Ge-Sb-Te phase-change memory materials. *Nat. Mater.* **7**, 399–405 (2008).
54. Akola, J. & Jones, R. O. Structural phase transitions on the nanoscale: The crucial pattern in the phase-change materials $Ge_2Sb_2Te_5$ and GeTe. *Phys. Rev. B* **76**, 235201 (2007).
55. Akola, J. & Jones, R. O. Structure of amorphous $Ge_8Sb_2Te_{11}$: GeTe-Sb_2Te_3 alloys and optical storage. *Phys. Rev. B* **79**, 134118 (2009).
56. Chen, Y. et al. Chemical understanding of resistance drift suppression in Ge-Sn-Te phase-change memory materials. *J. Mater. Chem. C.* **8**, 71–77 (2020).
57. Bernstein, N. et al. Quantifying chemical structure and machine-learned atomic energies in amorphous and liquid silicon. *Angew. Chem. Int. Ed.* **58**, 7057–7061 (2019).
58. Lee, B. S. et al. Observation of the role of subcritical nuclei in crystallization of a glassy solid. *Science* **326**, 980–984 (2009).
59. Matsunaga, T. et al. From local structure to nanosecond recrystallization dynamics in AgInSbTe phase-change materials. *Nat. Mater.* **10**, 129–134 (2011).
60. Ronneberger, I., Chen, Y., Zhang, W. & Mazzarello, R. Local structural origin of the crystallization tendency of pure and alloyed Sb. *Phys. Status Solidi RRL* **13**, 1800552 (2019).
61. Gabardi, S., Caravati, S., Bernasconi, M. & Parrinello, M. Density functional simulations of Sb-rich GeSbTe phase change alloys. *J. Phys. Condens. Matter* **24**, 385803 (2012).
62. Okugawa, M., Nakamura, R., Ishimaru, M., Yasuda, H. & Numakura, H. Thermal crystallization of sputter-deposited amorphous Ge films: Competition of diamond cubic and hexagonal phases. *AIP Adv.* **6**, 125035 (2016).
63. Privitera, S. M. S. et al. Crystallization properties of melt-quenched Ge-rich GeSbTe thin films for phase change memory applications. *J. Appl. Phys.* **128**, 155105 (2020).
64. Caravati, S. et al. First-principles study of nitrogen doping in cubic and amorphous $Ge_2Sb_2Te_5$. *J. Phys. Condens. Matter* **23**, 265801 (2011).

65. Salinga, M. et al. Monatomic phase change memory. *Nat. Mater.* **17**, 681–685 (2018).
66. Cheng, Z. et al. Antimony thin films demonstrate programmable optical nonlinearity. *Sci. Adv.* **7**, eabd7097 (2021).
67. Zhang, W. & Ma, E. Single-element glass to record data. *Nat. Mater.* **17**, 654–655 (2018).
68. Kühne, T., Krack, M., Mohamed, F. & Parrinello, M. Efficient and accurate Car-Parrinello-like approach to Born-Oppenheimer molecular dynamics. *Phys. Rev. Lett.* **98**, 066401 (2007).
69. Hutter, J., Iannuzzi, M., Schiffmann, F. & VandeVondele, J. cp2k: atomistic simulations of condensed matter systems. *WIREs Comput. Mol. Sci.* **4**, 15–25 (2014).
70. Goedecker, S., Teter, M. & Hutter, J. Separable dual-space Gaussian pseudopotentials. *Phys. Rev. B* **54**, 1703 (1996).
71. Perdew, J. P., Burke, K. & Ernzerhof, M. Generalized gradient approximation made simple. *Phys. Rev. Lett.* **77**, 3865–3868 (1996).
72. Kresse, G. & Hafner, J. Ab initio molecular dynamics for liquid metals. *Phys. Rev. B* **47**, 558–561 (1993).
73. Kresse, G. & Joubert, D. From ultrasoft pseudopotentials to the projector augmented-wave method. *Phys. Rev. B* **59**, 1758 (1999).
74. Cheng, B. et al. Mapping materials and molecules. *Acc. Chem. Res.* **53**, 1981–1991 (2020).
75. Deringer, V. L., Caro, M. A. & Csányi, G. Machine learning interatomic potentials as emerging tools for materials science. *Adv. Mater.* **31**, 1902765 (2019).
76. Mocanu, F. C. et al. Modeling the phase-change memory material $Ge_2Sb_2Te_5$ with a machine-learned interatomic potential. *J. Phys. Chem. B* **122**, 8998–9006 (2018).
77. Himanen, L. et al. DScribe: library ofdescriptors for machine learning in materials science. *Comput. Phys. Commun.* **247**, 106949 (2020).

ACKNOWLEDGEMENTS

W.Z. thanks the support of National Natural Science Foundation of China (61774123) and 111 Project 2.0 (BP2018008). R.M. acknowledges funding from Deutsche Forschungsgemeinschaft (DFG) within SFB 917 ('Nanoswitches'). V.L.D. acknowledges a Leverhulme Early Career Fellowship. The authors acknowledge the support by the HPC platform of Xi'an Jiaotong University, and the International Joint Laboratory for Micro/Nano Manufacturing and Measurement Technologies of Xi'an Jiaotong University.

AUTHOR CONTRIBUTIONS

W.Z. and L.S. conceptualized the work. The ab initio simulations were performed by Y.-X.Z. and L.S. The paper was written by W.Z. with input from V.L.D. and R.M. All authors contributed to the discussions and analyses of the data, and approved the final version.

COMPETING INTERESTS

The authors declare no competing interests.

ADDITIONAL INFORMATION

Supplementary information The online version contains supplementary material available at https://doi.org/10.1038/s41524-021-00496-7.

Correspondence and requests for materials should be addressed to W.Z.

Reprints and permission information is available at http://www.nature.com/reprints

Publisher's note Springer Nature remains neutral with regard to jurisdictional claims in published maps and institutional affiliations.

Open Access This article is licensed under a Creative Commons Attribution 4.0 International License, which permits use, sharing, adaptation, distribution and reproduction in any medium or format, as long as you give appropriate credit to the original author(s) and the source, provide a link to the Creative Commons license, and indicate if changes were made. The images or other third party material in this article are included in the article's Creative Commons license, unless indicated otherwise in a credit line to the material. If material is not included in the article's Creative Commons license and your intended use is not permitted by statutory regulation or exceeds the permitted use, you will need to obtain permission directly from the copyright holder. To view a copy of this license, visit http://creativecommons.org/licenses/by/4.0/.

© The Author(s) 2021